Aerodynamic Aspects of the Longitudinal Motion of a High-Lift Aircraft Configuration with Circulation Control

By D. Keller AND R. Rudnik

Institut für Aerodynamik und Strömungstechnik, Deutsches Zentrum für Luft- Raumfahrt
Lilienthalplatz 7, 38108 Braunschweig, Germany

The aim of subproject *C1* of the *Collaborative Research Center/ Sonderforschungsbereich 880* (*SFB 880*) is to investigate numerically the flight mechanical characteristics of an aircraft with circulation controlled high-lift devices from an aerodynamic point of view. This paper summarizes the most important aspects of the work done so far. It begins with a basic analysis of the impact of varying blowing coefficients on the aircraft performance based on the wing-body configuration. Furthermore, an overview of the influence of the circulation controlled wing on the aerodynamics of the horizontal tail plane is presented. Eventually, the resulting longitudinal static stability and controllability behavior of the *SFB 880*'s reference aircraft is discussed. Additionally, the interaction of a circulation controlled wing and the slipsteam of a wing mounted turboprop engine is investigated. Besides the studies of the static behavior, first results of the dynamic behavior, specifically the temporal behavior of circulation control after being activated are presented.

1. Introduction

The aerodynamic properties of circulation control have been studied intensively in the past [1–4]. Regarding aeronautical applications, most of these studies are of fundamental nature and focus on the potential of this technology to increase lift. Even though, in recent years, the test beds became more complex by investigating 3D flowfields and complete aircraft configurations [5–8], the aim of the investigations, i.e. the assessment of the capabilities remained rudimentary. The work of subproject C1 of the *SFB 880* is considered to shift the scope of aerodynamic investigations on circulation control to the next level by examining the effects, circulation control has on the handling qualities of an aircraft and to derive possible constraints regarding aircraft design. The results also improve a database, which enables the aircraft maneuver simulation and the development of a flight control system. Therefore, steady as well as unsteady Reynolds-Averaged-Navier-Stokes (RANS) simulations were performed. The work started with basic investigations. After performing mesh topology and grid convergence studies [9] in order to establish a best practice for the mesh generation of this kind of geometries, the fundamental behavior and interaction of a wing and horizontal tail plane were investigated in 2D with representative sections from the main wing and the horizontal tailplane (HTP) of the reference aircraft. Besides the assessment of the longitudinal static stability, unsteady calculations were performed to gain an idea of the dynamic behavior. This includes the estimation of dynamic derivatives as well as the start-up behavior when activating or deactivating the circulation control. The extension of the work into 3D again

began with a meshing study, which adressed wake resolution and was followed by a basic investigation of the aircraft specific blowing parameters. Afterwards, the longitudinal static stability and controllability of the reference aircraft with and without engine effects was evaluated. This paper focusses on the results of the 3D simulations and discusses the static behavior of the landing configuration and the impact of installed turboprop engines. Furthermore, the dynamic behavior after a sudden pressure rise within the plenum are examined.

2. Flow Solver

The calculations were performed with the *DLR TAU* code [10], which uses an unstructured finite volume approach for solving the Reynolds-averaged Navier-Stokes equations. For this investigation, the implicit LUSGS scheme was chosen for time stepping and a central scheme for the spatial discretization of the convective fluxes. The turbulence effects are modeled with the original Spalart-Allmaras formulation (SA) [11] with vortical and rotational flow correction based on the Spalart-Shur correction [12]. In order to model the turboprob engine, an actuator disk is implemented, which uses blade data from a 2D blade element theory. In this way, the local load of the propeller is calculated based on a given radial distribution of force coefficients along the blades and the local flow conditions.

3. Test Configuration

The aim of the *SFB 880* is to investigate the potential and challenges of a full aircraft configuration equipped with circulation control. Therefore, at the beginning of the project, a generic medium range aircraft with high wing was designed with the preliminary design tool *PrADO* [13]. Its mission range is set to around 2000km at a cruise mach number of $M_{\mathrm{cr}} = 0.74$ and maximum payload, which includes 100 passengers. A major design constraint was a maximum take off and landing distance of 800m. To achieve this, the aircraft is powered by turboprop engines, whereas the underlying blade data were provided by the *SFB 880* subproject A3 and evolved from a propeller design carried out in a related project [14]. Furthermore, it is equipped with a circulation controlled plain flap and aileron. For optimal efficiency of the circulation control, the plenum along the wing span is separated into six sections, which can be independently pressurized to adjust the blowing to the local flow conditions on the wing [9]. In landing configuration, which is discussed in this paper, the flap is deflected to 65° and the aileron is drooped by 45°, whereas the wing is unprotected at the leading edge. Figure 1(a) shows the geometry, as it is used for the CFD calculations.

Since the full model has to be simulated for the *one engine inoperative* (*OEI*) case in future, the number of mesh points had to be considered. Therefore, a hybrid mesh approach with *Centaur* [15], which was investigated before [9], was chosen to accurately and efficiently discretize the computational space. Here, the main challenge was to properly resolve the jet mixing area behind the plenum exit (Fig. 1(b)). Especially, the small slot height of $h_c = 0.0006c$ and the strongly varying velocities around the wing with

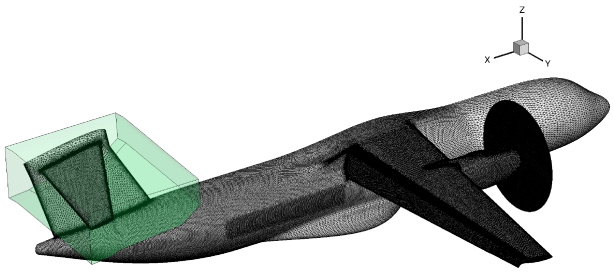

(a) Surface mesh

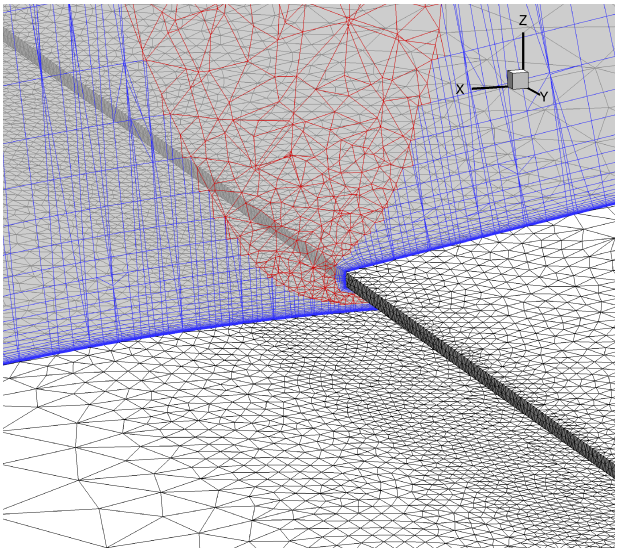

(b) Mesh topology at the jet exit

FIGURE 1. Mesh details

its impact on the requirements regarding the first cell height and final prism layer height, challenged the semi-automated meshing process. Special attention was also paid to the wing wake region as the flow condition at the tail plane plays an important role for flight mechanical evaluations.

In order to trim the aircraft with the least meshing influence, the mesh was built modularly. Thus, only the HTP module, which is illustrated by the green box in Fig. 1(a) has to be remeshed for changing the horizontal stabilizer's angle. The work resulted in a mesh family with around 37.5M points for the meshes of the half model.

For the simulation of the step responses, a representative 2D geometry was created. In order to represent the aerodynamic behavior, the airfoils reflect the sections of the main wing and the HTP at their locations of the mean aerodynamic chords both in shape and in chord length. Furthermore, the relative location of the elements to each other are taken from the 3D reference aircraft. However, in order to match the correct relation of forces and moments of the two airfoils, the resulting global coefficients of the HTP from

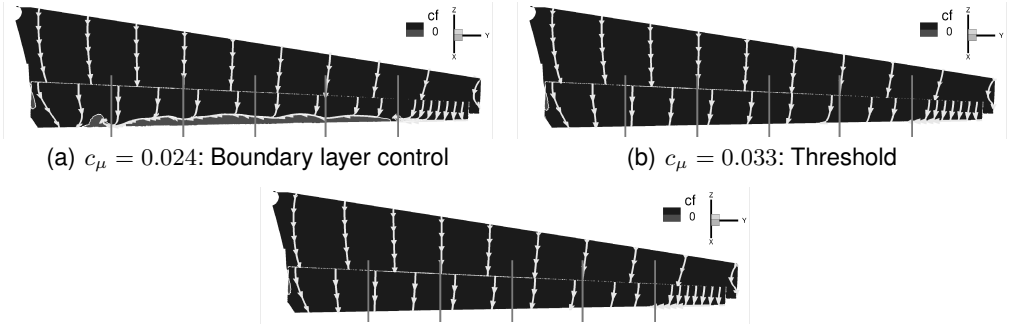

(a) $c_\mu = 0.024$: Boundary layer control (b) $c_\mu = 0.033$: Threshold

(c) $c_\mu = 0.045$: Super circulation

FIGURE 2. Friction coefficients and streamlines on the wing upper surface at $\alpha = 0.0^\circ$ for different operating points

the simulations are corrected by the ratio between the HTP span and the main wing span of the reference aircraft.

4. Computational Results

4.1. *Static behavior of the reference aircraft*

When employing circulation control on a flap, two different operating modes can be distinguished. At relatively low blowing coefficients, the flow on the flaps is not completely attached and the strength of the blown jet regulates the amount of separation. This usage is called boundary layer control and is the most effective way to utilize circulation control. After reaching fully attached flaps, additional blowing leads to so-called supercirculation, which is less effective. The threshold between these two utilization ranges is interesting, as it gives the maximum lift at good effectiveness. Figure 2 demonstrates the separation behavior in terms of the distribution of friction coefficients for three settings, which are characteristic for the different operating modes. At $c_\mu = 0.024$, the flow is partially separated from the flap, whereas it is fully attached for $c_\mu \geq 0.033$. The resulting lift coefficients (Fig. 3(a)) show, that the additional gain of lift due to increased blowing is reduced after $c_\mu = 0.033$ is reached. Figure 3(b) illustrates the distribution of lift coefficients over the angle of attack for the different blowing coefficients. Even though, the lift increases with rising blowing coefficients, the maximum angle of attack is reduced as well. The reason for this lies in the stall mechanism of the wing, which is identical for all investigated blowing coefficients. At $\alpha_{\max}$, the flow separates at the leading edge at $\eta \approx 0.7$, which indicates, that the aerodynamic limit of the leading edge is reached. At higher blowing coefficients, the wing circulation is higher and hence the velocities at the leading edge rise, as well. Thus, the limits of the leading edge geometry are reached earlier. Unlike typical high-lift devices, the circulation controlled flap produces less drag when it is partially separated and especially after it stalls (Fig. 3(c)). Besides the high proportion of induced drag, the reason for this can be also found in the high flap deflection and the resulting direction of the pressure forces. When the flow separates, the pressure rises in the separated region and exerts a horizontal force on the flap's upper surface.

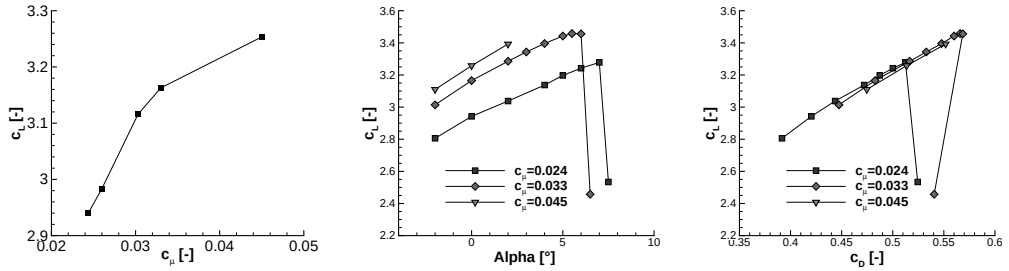

(a) Lift coefficients at $\alpha = 0^\circ$ for different blowing coefficients c_μ (b) Lift curves over angle of attack α (c) Lift over drag

FIGURE 3. Lift coefficients of wing-body configuration

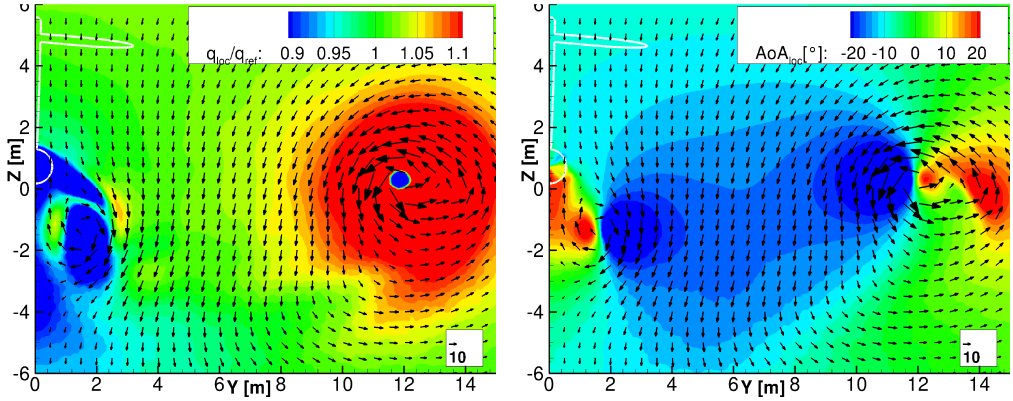

(a) Local dynamic pressure (b) Local angle of attack

FIGURE 4. Flowfield in cutplane through $c_{\mu,\mathrm{HTP}}/4$ at $\alpha = 0^\circ$ and $c_\mu = 0.045$

4.1.1. *Downwash Investigation*

For the longitudinal stability and controllability, the flowfield around the HTP is of particular importance. After performing a wake meshing study [9], the local dynamic pressure and angle of attack at the HTP was therefore investigated. Because of the high position of the HTP and the low vertical level of the main wing wake due to the high wing circulation, the local dynamic pressure at the HTP is nearly unaffected (Fig. 4(a)). However, the strong wing circulation leads to very high downwash angles, which are plotted in Fig. 4(b) for $c_\mu = 0.045$ and $\alpha = 0.0^\circ$. Figure 5(a) shows the downwash along the position of the quarter chord line of the HTP for the chosen blowing settings at $\alpha = 0^\circ$. The downwash increases strongly towards the HTP tip and depends on the blowing coefficient, as expected. Figure 5(b) compares the change of downwash due to a change in lift, originated from a varying angle of attack on one hand and a modified blowing coefficient on the other. It demonstrates, that the values of the gradients are lower and constant for lift increases due to increased blowing. The gradients for constant blowing get slightly steeper towards higher angles of attack because of the reduced distance between the main wing wake and the HTP position. The break down near $\alpha_{\max}$ is associated with a shift in the main wing loading and a resulting change in downwash distribution.

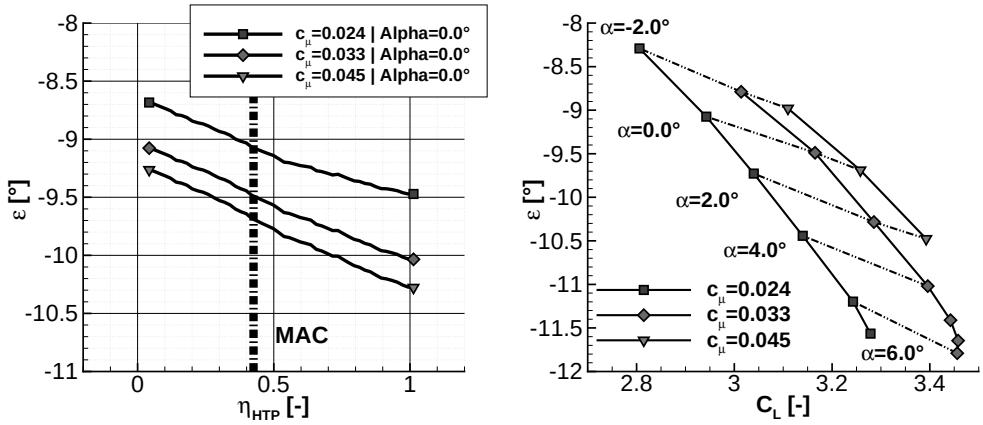

(a) Downwash at $\alpha = 0°$ along span at $c_{\mathrm{HTP}}/4$ line

(b) Change of downwash due to change in lift coefficient

FIGURE 5. Downwash at the horizontal tail plane position

4.1.2. *Stability and Controllability Investigation*

For the evaluation of the flight mechanical behavior of an aircraft, the longitudinal static stability and controllability are two fundamental characteristics. While the controllability demonstrate the possibility of trimming an aircraft at a certain position of center of gravity (c.g.), the longitudinal static stability indicates the behavior of an aircraft after a disturbance in the angle of attack. The investigation of the longitudinal stability and controllability for the landing configuration was performed at $c_\mu = 0.033$ and $\alpha = 0°$. Table 2 shows the controllability limits for the configuration, if the maximum HTP trim angle does not exceed $i_{\mathrm{HTP,max}} = \pm 8°$, as it was predefined in the preliminary design process. Furthermore, it demonstrates that the stability limit of the aircraft lies far behind the rearward limit of controllability. On the one hand, this means that the c.g. may lie behind the controllability limit without being unstable, if higher trim deflections are allowed and if they are aerodynamically feasible. On the other hand, it also means, that the aircraft will most likely be stiff, if it operates with the c.g. within the given range. The mean position of c.g. with respect to the mean aerodynamic center of the wing is located at $\frac{x_{\mathrm{cg,mid}}}{c_\mu} = -0.015$. Compared to the preliminary analysis of the cruise configuration, the mean position of c.g. is shifted by $\Delta\frac{x_{\mathrm{cg,mid}}}{c_\mu} = -22.9\%$ towards the front, which can be accounted to the strong downwash at the HTP position. Even though, the width of the range is also reduced by $\Delta\frac{x_{\mathrm{cg,range}}}{c_\mu} = 0.41$ due to high pitching moments of the wing, it is still comparably large with $\frac{x_{\mathrm{cg,range}}}{c_\mu} = 0.34$. This can be explained by the large relative horizontal tail volume and its good efficiency due to the undisturbed dynamic pressure. The mass analysis of the preliminary design study resulted in a most rearward position of the c.g. for maximum landing weight of $\frac{x_{\mathrm{cg}} - x_{\mathrm{MAC,WB}}}{c_\mu} = 0.31$, which is behind the most rearward controllability limit at $i_{\mathrm{HTP,max}} = \pm 8°$. However, Fig. 6 demonstrates its aerodynamic feasibility, whereas an HTP deflection of $i_{\mathrm{HTP}} = 16.2°$ is necessary to trim the aircraft. In this case, wing and fuselage contribute to a positive pitching moment, which requires the HTP to produce a negative pitching moment and consequently increase the overall lift of the aircraft. The aircraft's pitching moment coefficient declines with rising angle of attack until $\alpha_{\max}$ is reached. For angles higher than $\alpha_{\max}$, the gradient is positive, which indicates an unstable behavior. The reason lies in the stall mechanism

	$\frac{x_{cg}-x_{MAC,WB}}{c_\mu}$
Most foreward CoG position	0.16
Most rearward CoG position	0.31

TABLE 1. Center of gravitiy positions at maximum landing weight as result of loading variation

	$\frac{x_{cg}-x_{MAC,WB}}{c_\mu}$
Foreward controllability limit	-0.19
Rearward controllability limit	0.15
Stability limit	0.46

TABLE 2. Controllability and stability limits

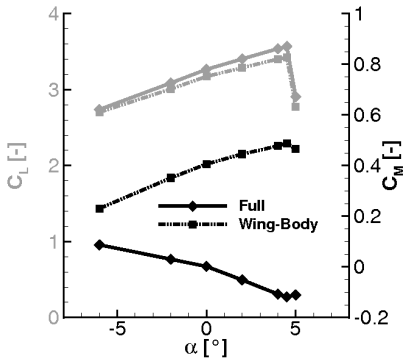

FIGURE 6. Global coefficients for trimmed reference aircraft

and the resulting circulation distribution along the wing. Even though, the wing is actually stable after stalling, the sudden rise of circulation in spanwise direction due to the separation leads to an additional vortex, which increases the downwash at the location of the HTP. This in turn results in an increased pitching moment.

4.1.3. *Engine influence on the behavior of the longitudinal motion*

For the calculation with engine, the aircraft was trimmed for a level flight at $\alpha = 0°$. In case of the most forward c.g. in landing configuration, this means an increase of the HTP trim angle by $\Delta i_{\mathrm{HTP,T1}} = 1.8°$ for the aircraft with nacelle and engine on, compared to the reference aircraft without nacelle. Thereby, the pitching moment of the propeller itself actually reduces the necessary horizontal stabilizer angle by $\Delta i_{\mathrm{HTP,T1,gross}} = -0.9°$. However, the influence of the thrust on the flow around the wing increases its pitching moment and leads to a higher downwash at the HTP, resulting in the higher trim angle of $i_{\mathrm{HTP,T1}} = 11.4°$.
In order to compensate the drag, the engine has to deliver a gross thrust of $T_{\mathrm{T1,gross}} =$

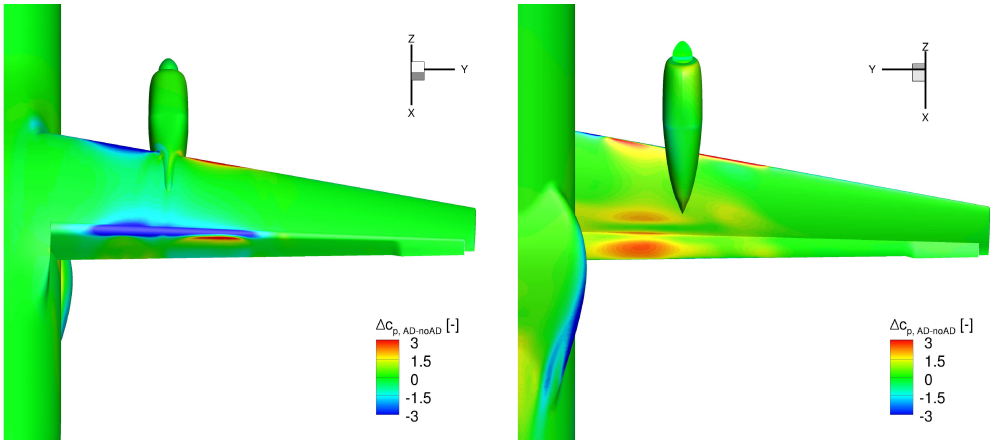

(a) Upper Surface (b) Lower Surface

FIGURE 7. Delta plots of the pressure coefficients

$55.95kN$ ($c_{\mathrm{t,T1,gross}} = 0.28$). The significant thrust requirement is due to the increased drag based on the interaction between the sliptream and the wing. The delta plots of pressure coefficients at the wing with thrust and without thrust (Fig. 7) show the increased suction peaks on the upper flap surface and at the inboard wing nose (Fig. 7(a)). On the wing's lower surface (Fig. 7(b)), the pressure coefficients around the nacelle and especially on the flap are strongly increased due to the accelerated flow of the slipstream. Therefore, the net thrust is only $c_{\mathrm{t,T1,net}} \approx 0.18$, which translates into an installation loss of around 37%. However, the influence of the slipstream also increases the lift coefficient by $\Delta c_{\mathrm{L,T1}} = 0.59$ to $c_{\mathrm{L,T1}} = 3.64$. The resulting lift to drag ratio is therefore reduced by $\Delta L/D_{\mathrm{T1}} = -1.6$ to $L/D = 5.0$.

4.2. *Dynamic behavior of Circulation Control*

The investigation of the time response to an activation and deactivation, respectively, of the circulation control was conducted with the representative 2D geometry. The geometry was therefore trimmed with the moment reference point representing the most rearward position of the reference aircraft's c.g. at maximum landing weight.

Figure 8 shows the evolution of the flowfield at $\alpha = 1.0°$ when activating the circulation control. At $t = 0s$, the pressure at the plenum is increased. However, the flow around the wing is not influenced yet. It separates early on the flap and vortex shedding can be seen behind the main airfoil. The local angle of attack at the HTP airfoil is similar to the global one. After $\Delta t = 0.26s$, the flow is already fully attached to the flap and the stagnation point at the nose moves along the lower surface side towards the rear, thus creating more circulation. Consequently, the velocities on the upper surface side are strongly increased. Due to the higher velocities of the jet wake, the low velocity wake of the formerly separated flap is moved towards the HTP, which leads to a slightly increased local angle of attack. At $t = 0.89s$, the velocity level on the upper side of the main airfoil increases even more. Now, the low velocity wake from the initially deactivated circulation control is completely carried away and the local angle of attack at the HTP is dominated by the high circulation of the main airfoil, resulting in a strong negative local angle of attack.

Figure 9 shows the step response of the lift and pitching moment coefficients to the

sudden increase of the plenum pressure. When activating the circulation control, the lift coefficient of the main wing quickly rises and reaches 90% of its maximum lift after $t = 0.33s$. The distribution equals a first order lag element (PT1) and therefore could be described with a time constant of $T_{\alpha=1^\circ} = 0.17s$ for $\alpha = 1^\circ$. The distribution of the lift coefficients of the HTP rather behave like a higher order lag element, whereas the overshoot and undershoot correlate with the wake evolution as discussed before.
Due to the reduced local angle of attack at the HTP, the final lift coefficient after the new state is reached, is lower than the initial one and thus changes the HTP's pitching moment in nose up direction. This gives additional relevance to the location of the moment reference point, i.e. the c.g. If the moment reference point is located rather towards the front, the change in pitching moments of the main airfoil and the HTP due to activation of the circulation control will cancel out each other to some extend. However, when moving the moment reference point towards the rear, from a certain point $P_{\mathrm{CC,N,MW}}$, the additional pitching moments of both elements will point into the same direction and therefore will lead to a comparably high nose up pitching moment, as it is the case here. At the threshold, where this happens, the algebraic sign of the main airfoil's additional pitching moment is zero and thus, this location is analogous to the neutral point of the main airfoil. However, it should be made clear that this does only apply for a certain point in time, e.g. after full transition to the new state. Between the initial and the final state, the pitching moment varies. In the investigated case, the point $P_{\mathrm{CC,N,MW}}$ lies at $x_{\mathrm{CC,N,MW}} = 0.43c_{\mathrm{MW}}$ (Fig. 10). The moment reference point obviously lies behind the threhold, and the additional pitching moments of main airfoil and HTP due to the activation of the circulation control add up to a comparably high final value. From $c_{\mathrm{m,MW+HTP}} = 0.0$ at $t = 0s$, the overall pitching moment rises to $c_{\mathrm{m,MW+HTP}} = 0.61$ at $t = 6s$. For the two element configuration, there can also be found a moment reference point $P_{\mathrm{CC,N,MW+HTP}}$, at which the overall pitching moment before and after activation is equal. Due to the different algebraic sign of the change of lift of the HTP in comparison to the change of lift of the main airfoil, this moment reference point has to lie in front of $x_{\mathrm{CC,N,MW}}$. If the moment reference point is located in front of $P_{\mathrm{CC,N,MW+HTP}}$, the configuration will have a pitch down tendency when the circulation control is being activated. If it lies behind $P_{\mathrm{CC,N,MW+HTP}}$, the configuration will have a pitch up tendency, which is less favourable as it leads to a higher angle of attack while the maximum angle of attack is reduced due to the blowing. For the investigated case, $P_{\mathrm{CC,N,MW+HTP}}$ is located at $x_{\mathrm{CC,N,MW+HTP}} = 0.31c_{\mathrm{MW}}$.
The step response of a sudden deactivation of the circulation control (Fig. 9(b)) behaves very similar to an activation. The coefficients of the main wing react quickly, whereas the coefficients of the HTP lag to the final values.

5. Conclusions

After identifying the basic aerodynamic characteristics of the reference aircraft's landing configuration, the influence of circulation control on the longitudinal static stability and controllability was investigated. The high circulation of the main wing results in a strong downwash at the HTP position, which is not only dependent on the amount of lift itself, but also on the way it is generated. Due to the downwash, the necessary HTP angles for trimming the aircraft are increased, or in other words, the range of controllable center of gravity positions will shift towards the front, if the possible angles of the horizontal stabilizer are limited to a certain range. This means for the investigated configuration

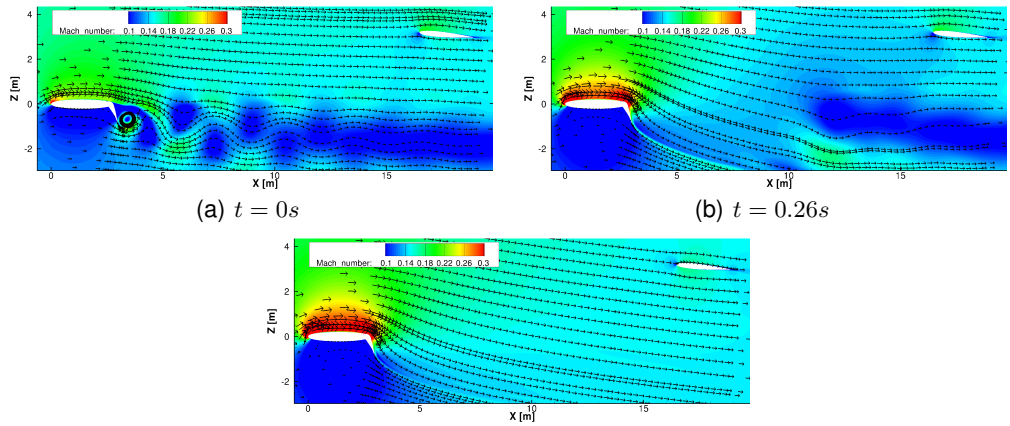

(a) $t = 0s$ (b) $t = 0.26s$

(c) $t = 0.89s$

FIGURE 8. Flowfield evolution after the activation of the circulation control

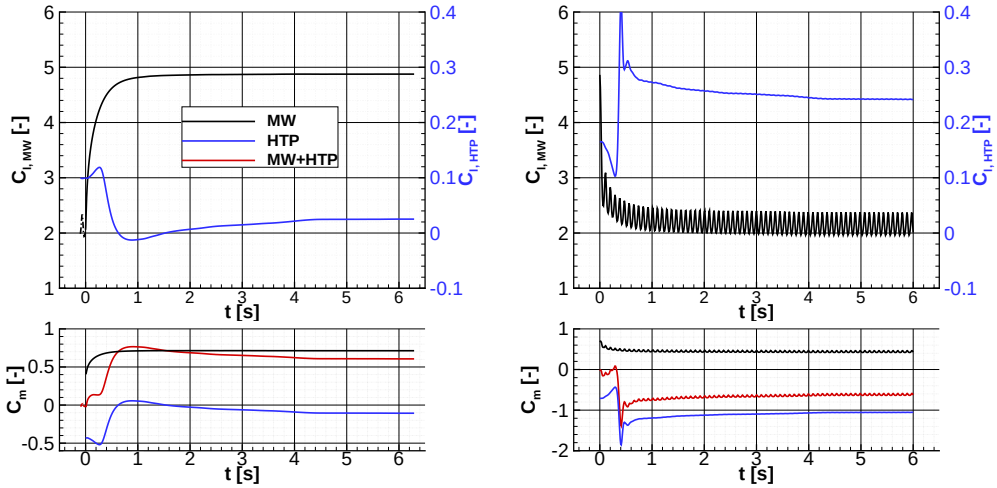

(a) Activation (b) Deactivation

FIGURE 9. Step response of lift and pitching moment coefficients to a pressure step in the plenum

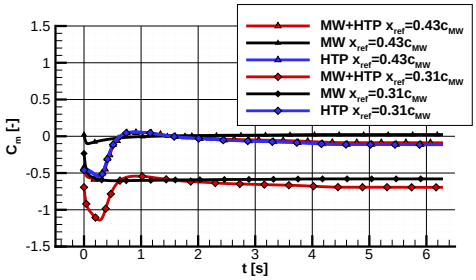

FIGURE 10. Pitching moment coefficients for different moment reference points

that the range of c.g. positions from the preliminary mass analysis is only feasible, if the range of possible HTP angles is extended to higher positive values. However, despite the high pitching moment of the main wing, the width of the center of gravity range is comparably large, which can be accounted to the big relative HTP volume on one hand and the undisturbed local dynamic pressure at the HTP on the other.
The calculations with installed engines showed, that the slipstream has a big impact on the pressure distribution of the main wing. On the one hand, this gives the opportunity to increase the lift coefficient significantly. On the other hand, the drag rises as well, leading to a lower lift to drag ratio. The modified flow around the wing is also accompanied by higher pitching moments and downwash angles at the HTP, which result in higher stabilizer trim angles.
The simulation of the activation and deactivation of the circulation control demonstrated, that the main airfoil responds fairly quickly. However, the coefficients of the downstream located HTP airfoil fluctuate until the change in the wake due to the changed blowing pass the HTP. The impact on the pitching moment coefficient depends on the location of the moment reference point. For the case of activation, it was shown, that for a certain position, the initial pitching moment of the main airfoil is identical to the final one. If the moment reference point is located behind this position, the pitching moments of the main wing and the HTP airfoil accumulate and result in a large nose-up pitching moment. If the moment reference point lies before the threshold, the pitching moments of the different elements cancel each other out to some extend. Again a location can be identified, where the sum of the initial pitching moments of both elements is identical to the sum after activation. For moment reference points which are located before or behind this point the sum of additional pitching moments from the activation will be negative or positive, respectively.
In the near future, the impact of the propeller slipstream on the aerodynamics of the aircraft will be studied in more detail. As part of this, the failure case *one engine inoperative* (*OEI*) will be investigated. Furthermore, unsteady simulations of the reference aircraft will be performed in order to determine the dynamic derivatives of the longitudinal motion.

Acknowledgments

References

[1] ENGLAR, R. J., BLAYLOCK, G. M. AND GAETA, R. J. (2010). Recent Experimental Development of Circulation Control Airfoils and Pneumatic Powered-Lift Systems. *AIAA Paper, 2010-345*.

[2] KORBACHER, G. K. (1974). Aerodynamics of powered high-lift systems. *Annual Review of Fluid Mechanics*, 319-358.

[3] PFINGSTEN, K.-C., JENSCH, C., KÖRBER, K. W. AND RADESPIEL, R. (2007). Numerical Simulation of the Flow around Circulation Control Airfoils. *First CEAS European Air and Space Conference*, Berlin, Germany.

[4] ALLAN, B. G., JONES, G. S. AND LIN, J. C. (2011). Reynolds-Averaged Navier-Stokes Simulation of a 2D Circulation Control Wind Tunnel Experiment. *AIAA Paper*.

[5] PFINGSTEN, K.-C., JENSCH, C., KÖRBER, K. W. AND RADESPIEL, R. (2007). Numerical Simulation of a Wing with a Gapless High-Lift System Using Circulation Control. *Notes on Numerical Fluid Mechanics and Multidisciplinary Design*.

[6] MARSHALL, D. D. AND JAMESON, K. K. (2010). Overview of Recent Circulation Control Modeling Activities at Cal Poly. *AIAA Paper*, 2010-348.

[7] PETROV, A. V. (2012). Aerodynamics of STOL Airplanes with Powered High-Lift Systems. *Proceedings of the 28th International Congress of the Aeronautical Sciences*.

[8] BURNAZZI, M., RADESPIEL, R. AND KELLER, D. (2012). Numerical simulation of a 3D aircraft model equipped with active Coanda high-lift devices. *Proceedings of the 18th DGLR-STAB Symposium*, Stuttgart, Germany.

[9] KELLER, D. (2012). Numerical Investigation of the Longitudinal Static Stability of a Transport Aircraft with Circulation Control. *Proceedings of the 18th DGLR-STAB Symposium*, Stuttgart, Germany.

[10] GERHOLD, T. (2005). Overview of the Hybrid RANS Code TAU. *Notes on Numerical Fluid Mechanics and Multidisciplinary Design*, Ger.

[11] SPALART, P., R. AND ALLMARAS S. R. (1992). A One–Equation Turbulence Model for Aerodynamic–Flows. *AIAA Paper*, 92–0439.

[12] SPALART, P. R. AND SHUR M. (1997). On the sensitization of turbulence models to rotation and curvature. *Aerospace Science and Technology*.

[13] HEINZE, W., ÖSTERHELD, C. M. AND HORST, P. (2001). Multidisziplinäres Flugzeugentwurfsverfahren PrADO - Programmentwurf und Anwendung im Rahmen von Flugzeug-Konzeptstudien. *DGLR-Jahrbuch 2001*.

[14] LENFERS, C. (2012). Propeller Design for a future QESTOL Aircraft in the BNF Project. *AIAA Paper* 2012–3334.

[15] CENTAURSOFT (retrieved 19th November 2012). Centaur Hybrid Grid Generation System. online web site, URL: http://www.centaursoft.com.